MODAL STRUCTURE OF PLATE BOUNDARIES AND KLEIN BOTTLE REVERBERATION

Jin Woo Lee and Mark Rau

Research Laboratory of Electronics
Massachusetts Institute of Technology
Cambridge, MA, USA
{jnlee | mrau}@mit.edu

ABSTRACT

Physical modeling sound synthesis has achieved remarkable success in terms of its fidelity to reality. In many cases, since modeling of the physical system is performed on the sounding objects that already exist in the real world, observation precedes the model itself. Departing from this convention, this paper aims to physically model the acoustic characteristics of objects that do not necessarily exist in reality. Specifically, we study wave propagation on compact two-dimensional (2D) manifolds that are non-orientable surfaces, such as the Klein bottle that cannot be embedded in three-dimensional Euclidean space without self-intersection. We derive closed-form expressions for the eigenfrequencies and mode shapes of non-orientable 2D topologies and study their acoustic characteristics. The modal structures are verified through comparison with finite-difference time-domain simulations. The results demonstrate how the topological character formed by the boundaries influences the acoustic resonances, and how the quotient-space framework provides a practical route to reverb synthesis on geometries with no physical counterpart.

1. INTRODUCTION

Physical modeling sound synthesis seeks to replicate acoustic phenomena by formulating and solving the governing equations of vibrating systems [1, 2]. The fundamental philosophy is to encode the physical system of sound generation into a set of equations, and then to solve them, either analytically or numerically [3, 4].

Among the most widely used physical modeling techniques are modal synthesis, which represents the acoustic response as a superposition of eigenmodes [1], and finite-difference time-domain (FDTD) methods, which discretize the wave or plate equation directly on a spatial grid [4, 5]. One representative example is the modeling of plate reverberation, which has been approached using both modal synthesis and FDTD methods [6]. Beyond modal synthesis and FDTD for reverberation, a variety of physical modeling methods have achieved high-fidelity results across a broad range of instruments: stringed instruments [7–10], woodwind instruments [11], struck membranes [12], and a variety of everyday objects [13–15]. In most cases, the model is anchored in a physical object that exists in the world, *i.e.*, its geometry, boundary conditions (BCs), and material properties are observed, measured, and then encoded to replicate the sound of that object. This convention, that observation precedes the model, has proven enormously productive, even allowing the sound synthesis of objects that are non-existent in reality in the sense that one can freely manipulate the physical properties of the virtual string and its length [16]. Yet, the model is still grounded in the physics of a real-world string, and the geometry of the sounding object is still constrained to be one that can be realized in three-dimensional Euclidean space. Therefore, if the governing equation is modeled by emulating the system of an actual musical instrument, while it could be difficult to realize in reality, it is not entirely impossible.

Departing from this convention, the present paper explores the wave propagation of non-orientable topology and its potential for sound synthesis of objects that are impossible in the real world. Investigations on characterizing the physical properties of non-orientable surfaces have been conducted in various fields, such as optical simulation [17], topological elasticity of non-orientable ribbons [18], spin-wave resonances in Möbius-strip nanostructures [19, 20], and geometry processing of impossible objects in computer graphics [21]. However, the acoustic consequences of non-orientable topology, and their potential for sound synthesis, have not been investigated in depth.

To investigate wave propagation and acoustic properties in non-orientable topology, we begin by exploring the acoustic characteristics associated with BCs that appear frequently in the field of acoustics. As the simplest examples of this, rectangular plates with Dirichlet and Neumann BCs are studied. Next, we derive the modes for a rectangle subject to periodic BCs and for its corresponding torus; we then introduce a method for calculating these modes that leverages tiling on this quotient space, along with the associated topological equivariance. We apply the same approach to non-orientable manifolds, such as a Möbius strip by constructing the modes by introducing a phase-conjugating periodic BC (formed by a reversal in the direction of the periodic BC). Finally, by extending the method for calculating modes on non-orientable manifolds, we determine the acoustic modes for shapes that cannot exist within three-dimensional Euclidean space, such as the Klein Bottle and the real projective plane.

In this paper, a modal analysis is conducted on a quotient space for wave propagation on 2D manifolds with the aforementioned BCs. As a result, explicit derivations of the mode structures and eigenfrequencies for the wave propagation on Möbius strip, Klein bottle, and real projective plane are presented. The derived mode structures and eigenfrequencies are verified through numerical simulations, demonstrating the consistency of the theoretical predictions with computational results. Discussion on the mode distribution change against the various BCs, and implications for acoustic design and reverberation modeling in non-orientable spaces are also provided.

2. WAVE PROPAGATION ON 2D MANIFOLDS AND QUOTIENT SPACES

We consider the acoustic wave equation on a two-dimensional manifold S,

$$\partial_t^2 p(\mathbf{r}, t) = c^2 \Delta_S p(\mathbf{r}, t), \tag{1}$$

where p is the scalar pressure field on space $\mathbf{r}$ and time t, with the wave speed c, and Δ_S is the scalar Laplacian on S. For a stationary geometry, the system admits separable eigensolutions

$$p_{mn}(\mathbf{r}, t) = \phi_{mn}(\mathbf{r}) \big[A_{mn} \cos(\omega_{mn} t) + B_{mn} \sin(\omega_{mn} t)\big], \tag{2}$$

with the initial pressure and velocity coefficients A_{mn} and B_{mn}, and the eigenfrequencies ω_{mn}. The spatial modes ϕ_{mn} satisfy the Helmholtz eigenvalue problem

$$\Delta_S\, \phi_{mn} + k_{mn}^2\, \phi_{mn} = 0, \qquad \omega_{mn} = c\, k_{mn}. \tag{3}$$

Finding the resonant structure of S reduces to solving Equation (3), where the wavenumber k_{mn} and the mode shapes ϕ_{mn} can be determined by the initial and boundary conditions.

While various acoustic BCs exist, the simplest examples among them are the Dirichlet and Neumann types. The Dirichlet condition fixes ϕ at the boundary by zero, while the Neumann condition fixes the normal derivative by zero. Waves passing through this boundary undergo a phase reversal and a change in their direction of propagation. For this reason, Dirichlet and Neumann BCs are often regarded as boundaries that mirror the phase; specifically, Dirichlet conditions may be viewed as a reflection that inverts the sign of the reflected scalar, whereas Neumann conditions may be seen as a reflection that preserves the sign.

Another important class of BCs is the periodic type, which identifies opposite edges of a rectangular domain. As the name implies, a periodic BC specifies the rule that one boundary is identical to the other. Specifically, periodic BCs are further categorized based on whether the direction of travel of the points deemed identical is preserved or reversed. The usual periodic BC, as in the torus, identifies opposite edges with matching orientation, meaning that a point traveling across the boundary continues in the same direction on the other side. In contrast, a phase-conjugating periodic BC, as seen in the Klein bottle and real projective plane, identifies opposite edges with reversed orientation, meaning that a point traveling across the boundary is reflected back in the opposite direction on the other side. A phase-conjugating periodic boundary gives rise to a non-orientable manifold and fundamentally alters the mode structure relative to the orientable case.

The BCs described above provide a direct recipe for tiling the plane: each rule acts as a generator that relates a fundamental domain $\sigma = [0, L_x] \times [0, L_y]$ to an adjacent copy, filling $\mathbb{R}^2$ with a regular σ-tiling. The Dirichlet and Neumann boundaries tile by reflections (with a sign flip ($\phi \to -\phi$) and without ($\phi \to +\phi$), respectively) while the four periodic geometries identify opposite edges of σ directly: the torus by pure translations, $(x, y) \sim (x{+}L_x,\, y)$ and $(x, y) \sim (x,\, y{+}L_y)$; the Möbius strip by a translation with transverse flip, $(x, y) \sim (x{+}L_x,\, L_y{-}y)$; the Klein bottle by one matched and one flipped pair, $(x, y) \sim (x{+}L_x,\, y)$ and $(x, y) \sim (-x,\, y{+}L_y)$; and the real projective plane by two flipped pairs, $(x, y) \sim (x{+}L_x,\, -y)$ and $(x, y) \sim (-x,\, y{+}L_y)$. Each such tiling is equivalently a *quotient space*: $\mathbb{R}^2$ modulo the equivalence relation imposed by the identification rules, and the mode shapes and eigenfrequencies for all six geometries are summarized in Table 1.

This construction extends well beyond the familiar geometries of three-dimensional space. Identifications that include an orientation reversal yield non-orientable manifolds such as the Möbius strip, Klein bottle, and $\mathbb{RP}^2$, some of which cannot be embedded in $\mathbb{R}^3$ without self-intersection, yet are perfectly well-defined as flat quotient spaces of the rectangle. The tiling picture therefore provides a computationally transparent route to simulating wave propagation on any of these manifolds: rather than working on a curved or self-intersecting surface, one solves the Helmholtz Equation (3) on the flat domain σ with the appropriate identification at each edge, and the eigenfunctions are exactly the spatial modes of the corresponding manifold.

3. MODE STRUCTURES

Each identification rule in the previous section translates into two simultaneous constraints on the spatial modes. For a given manifold S, a mode ϕ_{mn} on S follows from a superposition of plane waves on $\mathbb{R}^2$ that satisfy two conditions: first, the lattice periodicity that arises from the tiling restricts the Fourier support of ϕ_{mn} to the reciprocal lattice Λ^*, which is the set of wave vectors (k_x, k_y) compatible with the tiling period; second, the Helmholtz equation on $\mathbb{R}^2$ requires that $k_x^2 + k_y^2 = k_{mn}^2$. The allowed wave vectors then become the finite intersection of Λ^* with a circle of radius k_{mn}, and each spatial mode is a finite superposition of the corresponding plane waves:

$$\phi_{mn}(x, y) = \sum_{j=1}^{M} A_j\, e^{i(k_{xj} x + k_{yj} y)}. \tag{4}$$

Imposing the identification rules according to the BCs further constrains the allowed combinations of plane waves, and therefore the mode shapes and eigenfrequencies.

Table 1 summarizes the complete mode structures for each manifold. The table visualizes the manifold shapes and their quotient-space with σ-tilings, and lists the explicit mode shapes ϕ_{mn} and eigenfrequencies $f_{mn} = \omega_{mn}/(2\pi)$ for each geometry. Mode indices m, n are non-negative integers unless stated otherwise. The fundamental domain σ with size $L_x \times L_y$ is highlighted as an orange rectangle with an example wave pattern plotted in a red circle marker. The mode shapes are normalized to unit energy over the fundamental domain σ. On its tiled copies, the reflected copies of the example wave are shown in blue or red markers, where the color indicates the sign of the mode. The Dirichlet BC is depicted using a black solid line, mirroring the wave images with sign flips. The Neumann BC is shown by a gray dashed line mirroring the images but with no sign flips. The periodic BCs of $\mathbb{T}^2$, $\mathcal{K}$, and $\mathbb{RP}^2$ are shown in colored arrows, where the arrow direction indicates the orientation of the boundary and the color indicates whether the boundary is for the x- or y-direction. It is worth noting that the periodic BCs neither mirror the wave images nor flip their signs, but simply repeat the images across the boundaries according to the indicated orientations.

As previously explained, the mode construction presented in this paper is based on tiling arising from periodicity and equivariance governed by wave propagation rules at the boundaries. It is the phase-conjugating periodic boundary that introduces a non-trivial modification to this tiling; the presence or absence of such a boundary distinguishes between cases where the direction of the manifold's normal vector is uniquely defined (orientable) and those where it is not (non-orientable).

Table 1: Spatial modes, eigenfrequencies, and index conditions for 2D geometries. L_x, L_y: domain dimensions; c: wave speed.

Name	Topological Schematics	σ-tiling	f_{mn}	$\phi_{mn}(x,y)$
Rectangle (Dirichlet)		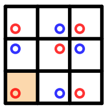	$\frac{c}{2}\sqrt{\frac{m^2}{L_x^2}+\frac{n^2}{L_y^2}}$	$\frac{2}{\sqrt{L_xL_y}}\sin\left(\frac{m\pi x}{L_x}\right)\sin\left(\frac{n\pi y}{L_y}\right)$
Rectangle (Neumann)		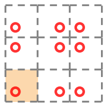	$\frac{c}{2}\sqrt{\frac{m^2}{L_x^2}+\frac{n^2}{L_y^2}}$	$\sqrt{\frac{1}{L_x^{(2)}L_y^{(2)}}}\cos\left(\frac{m\pi x}{L_x}\right)\cos\left(\frac{n\pi y}{L_y}\right)$
Torus ($\mathbb{T}^2$)	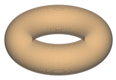	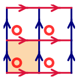	$c\sqrt{\frac{m^2}{L_x^2}+\frac{n^2}{L_y^2}}$	$\frac{1}{\sqrt{L_xL_y}}\exp\left[2\pi i\left(\frac{mx}{L_x}+\frac{ny}{L_y}\right)\right]$
Möbius Strip ($\mathcal{M}$)	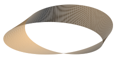	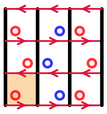	$\frac{c}{2}\sqrt{\frac{m^2}{L_x^2}+\frac{n^2}{L_y^2}}$	$\sqrt{\frac{2}{L_xL_y}}\sin\left(\frac{m\pi x}{L_x}\right)\exp\left(\frac{i\pi ny}{L_y}\right)$
Klein Bottle ($\mathcal{K}$)	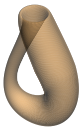	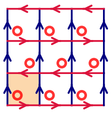	$\frac{c}{2}\sqrt{\frac{4m^2}{L_x^2}+\frac{n^2}{L_y^2}}$	$\sqrt{\frac{2}{L_x^{(1)}L_y}}\cos\left[\pi\left(\frac{2mx}{L_x}-\frac{n}{2}\right)\right]\exp\left(\frac{i\pi ny}{L_y}\right)$
Real Projective Plane ($\mathbb{RP}^2$)	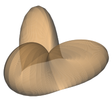	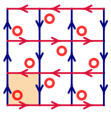	$\frac{c}{2}\sqrt{\frac{m^2}{L_x^2}+\frac{n^2}{L_y^2}}$	$\frac{2}{\sqrt{L_x^{(1)}L_y^{(1)}}}\cos\left[\pi\left(\frac{mx}{L_x}-\frac{m+n}{2}\right)\right]\cos\left[\pi\left(\frac{ny}{L_y}+\frac{m+n}{2}\right)\right]$

3.1. Orientable Manifolds

In each geometry in this category, the surface normal vector is well-defined and the manifold is orientable.

3.1.1. Dirichlet Rectangle

The sign-reversing reflection at both boundary pairs tiles $\mathbb{R}^2$ with period $2L_x \times 2L_y$, alternating the sign of ϕ with each reflection. Periodicity of the mode constrains the allowed wavenumbers to

$$k_x = \frac{m\pi}{L_x}, \quad k_y = \frac{n\pi}{L_y}, \quad m,n \geq 0,\ (m,n) \neq (0,0). \tag{5}$$

The modes with $m = 0$ or $n = 0$ will have $\phi = 0$ everywhere.
Mode and Eigenfrequency. The sign flip under $x \to -x$ forces the x-component to be anti-symmetric (sine), and similarly for y. The mode shapes are therefore the product of two sine functions:

$$\phi_{mn}(x,y) = \frac{2}{\sqrt{L_xL_y}}\sin\left(\frac{m\pi x}{L_x}\right)\sin\left(\frac{n\pi y}{L_y}\right). \tag{6}$$

The eigenfrequencies f_{mn} are given by the Pythagorean relation for the wavenumbers. All index pairs with $m, n \geq 1$ are present.

3.1.2. Neumann Rectangle

The tiling is the same as the Dirichlet case, but with no sign change at each reflection. The allowed wavenumbers are the same as the Dirichlet case.
Mode and Eigenfrequency. The no-flip condition forces each component to be symmetric (cosine); the index set includes the axes ($m = 0$ or $n = 0$), corresponding to modes uniform along one dimension:

$$\phi_{mn}(x,y) = \sqrt{\frac{1}{L_x^{(2)}L_y^{(2)}}}\cos\left(\frac{m\pi x}{L_x}\right)\cos\left(\frac{n\pi y}{L_y}\right), \tag{7}$$

where $L_x^{(2)} = L_x(2 - \delta_{m=0})$ with $\delta_{m=0}$ the Kronecker delta, and similarly for $L_y^{(2)}$. The eigenfrequencies f_{mn} are given identically to the Dirichlet case, and the two geometries differ only in mode parity and index set.

3.1.3. Torus

The pure translation in both directions tiles $\mathbb{R}^2$ with primitive vectors $(L_x, 0)$ and $(0, L_y)$, the same periods as σ itself; no reflections occur. Periodicity directly constrains the allowed wavenumbers to

$$k_x = \frac{2m\pi}{L_x}, \quad k_y = \frac{2n\pi}{L_y}, \quad m,n \in \mathbb{Z}. \tag{8}$$

Mode and Eigenfrequency. No sign-flip constraint is imposed, so the full complex-exponential basis is retained; modes at (m, n) and $(-m, -n)$ are complex conjugates sharing the same eigenfrequency, giving at least double degeneracy:

$$\phi_{mn}(x,y) = \frac{1}{\sqrt{L_xL_y}}\exp\left[2\pi i\left(\frac{mx}{L_x}+\frac{ny}{L_y}\right)\right]. \tag{9}$$

f_{mn} are given similarly to the rectangles, but with halved wavenumber spacing. (Notice the c instead of $c/2$ in the torus case.) So the frequency scale is doubled, but the index set is now the full integer lattice, so the torus spectrum is denser than the rectangle's and includes all of its modes as a subset (those with even m and n).

3.2. Non-orientable Manifolds

In each geometry in this category, at least one orientation-reversing identification is present, so the normal vector is *not* uniquely determined and the manifold is non-orientable.

3.2.1. Möbius Strip

$\mathcal{M}$ is formed by the identification $(x, y) \sim (x{+}L_x,\ L_y{-}y)$, translating L_x in x reflects the transverse coordinate $y \to L_y - y$. Applying this identification twice in either direction returns to the original orientation, so the σ-tiling of $\mathbb{R}^2$ has lattice periods $2L_x$ in x and $2L_y$ in y. Periodicity of the lifted mode with respect to this lattice constrains the allowed wavenumbers to

$$k_x = \frac{m\pi}{L_x}, \quad k_y = \frac{n\pi}{L_y}, \quad m, n \in \mathbb{Z}. \tag{10}$$

Mode and Eigenfrequency. The orientation-reversal in x forces the mode to be anti-symmetric under the x-translation by L_x, selecting the sine basis in x; the y-direction is only translated, so the complex-exponential basis is retained there:

$$\phi_{mn}(x, y) = \sqrt{\frac{2}{L_x L_y}} \sin\left(\frac{m\pi x}{L_x}\right) \exp\left(\frac{i\pi n y}{L_y}\right). \tag{11}$$

For Möbius strip modes, the combined anti-periodicity

$$\phi_{mn}(x{+}L_x, y{+}L_y) = -\phi_{mn}(x, y) \tag{12}$$

enforces $m{+}n$ to be odd. More details can be found in Appendix. Substituting Equation (10) into $\omega_{mn} = ck_{mn}$ and $k_{mn}^2 = k_x^2{+}k_y^2$:

$$f_{mn} = \frac{c}{2}\sqrt{\frac{m^2}{L_x^2} + \frac{n^2}{L_y^2}}, \qquad m + n \text{ odd}. \tag{13}$$

The frequency scale matches the Dirichlet rectangle, but the index restriction ($m + n$ odd) produces a sparser, atypical resonance set.

3.2.2. Klein Bottle

$\mathcal{K}$ has two independent identifications: $(x, y) \sim (x{+}L_x,\ y)$ (same orientation) and $(x, y) \sim (-x,\ y{+}L_y)$ (orientation-reversing). The first gives x-periodicity with period L_x directly; the second flips x while translating L_y in y, so two applications are needed to return to the same orientation, yielding y-lattice period $2L_y$. The allowed wavenumbers are therefore

$$k_x = \frac{2m\pi}{L_x}, \quad k_y = \frac{n\pi}{L_y}, \quad m, n \in \mathbb{Z}. \tag{14}$$

Note that k_x has half the spacing of the Möbius or rectangle cases (period L_x instead of $2L_x$), while k_y shares the same period $2L_y$.
Mode and Eigenfrequency. The equivariance condition in $\mathcal{K}$,

$$\phi(-x,\ y{+}L_y) = (-1)^n \phi(x, y), \tag{15}$$

yields a cosine basis in x with a half-integer phase offset that depends on n: when n is even, the mode is symmetric in x; when n is odd, the mode is anti-symmetric in x. The normalized mode is

$$\phi_{mn}(x, y) = \sqrt{\frac{2}{L_x L_y^{(1)}}} \cos\left[\pi\left(\frac{2mx}{L_x} - \frac{n}{2}\right)\right] \exp\left(\frac{i\pi n y}{L_y}\right), \tag{16}$$

where $L_y^{(1)} = L_y(1 + \delta_{m=0})$ is a length accounting for the $m = 0$ modes that are uniform in x and therefore have double the energy of the other modes, which have two symmetric peaks in x.

The $m = 0$ modes are special: they are uniform in x, so the x-flip has no effect and the mode is purely cosine-like regardless of n; for $m \neq 0$, the x-flip selects the cosine basis, but the phase shift couples the parity to n, giving a sine-like factor when n is odd. When n is even the x-factor is cosine-like; when n is odd it is sine-like. The eigenfrequency is obtained by substituting Equation (14):

$$f_{mn} = \frac{c}{2}\sqrt{\frac{4m^2}{L_x^2} + \frac{n^2}{L_y^2}}. \tag{17}$$

The factor of 4 on the m^2 term reflects the halved k_x spacing: low-order x-modes are pushed to higher frequencies compared to all other cases.

3.2.3. Real Projective Plane

$\mathbb{RP}^2$ has *both* pairs of edges identified with orientation reversal: $(x, y) \sim (x{+}L_x,\ -y)$ and $(x, y) \sim (-x,\ y{+}L_y)$. Each identification requires two traversals to restore orientation, so both x and y acquire a lattice period of $2L_x$ and $2L_y$ respectively. The wavenumbers are

$$k_x = \frac{m\pi}{L_x}, \quad k_y = \frac{n\pi}{L_y}, \quad m, n \in \mathbb{Z}, \tag{18}$$

identical in form to the Dirichlet rectangle, but the equivariance conditions under the two identifications are different.

$$\phi(x{+}L_x,\ -y) = (-1)^n\, \phi(x, y) \tag{19}$$
$$\phi(-x,\ y{+}L_y) = (-1)^m\, \phi(x, y) \tag{20}$$

Mode and Eigenfrequency. Both identifications include a spatial reflection, so both x- and y-components must be real even combinations (cosines), unlike the Möbius and Klein cases. Coupling the two reflections introduces independent phase offsets; the normalized mode satisfying Equation (19) and Equation (20) is

$$\phi_{mn}(x, y) = \sqrt{\frac{2}{L_x^{(1)} L_y^{(1)}}} \cos\left[\pi\left(\frac{mx}{L_x} - \frac{m+n}{2}\right)\right] \cos\left[\pi\left(\frac{ny}{L_y} + \frac{m+n}{2}\right)\right], \tag{21}$$

where $L_x^{(1)} = L_x(1 + \delta_{m=0})$ and $L_y^{(1)} = L_y(1 + \delta_{n=0})$ account for the $m = 0$ and $n = 0$ modes that are uniform in x or y and therefore have double the energy of the other modes. From Equation (18), the frequency formula is identical to the rectangle:

$$f_{mn} = \frac{c}{2}\sqrt{\frac{m^2}{L_x^2} + \frac{n^2}{L_y^2}}. \tag{22}$$

The resonance frequencies of $\mathbb{RP}^2$ are therefore co-spectral with the Neumann rectangle, but the mode shapes are distinct: the phase offsets $\pi(m{+}n)/2$ in both cosines produce modes that are neither purely even nor purely odd, and couple m and n in a way that has no rectangle analogue.

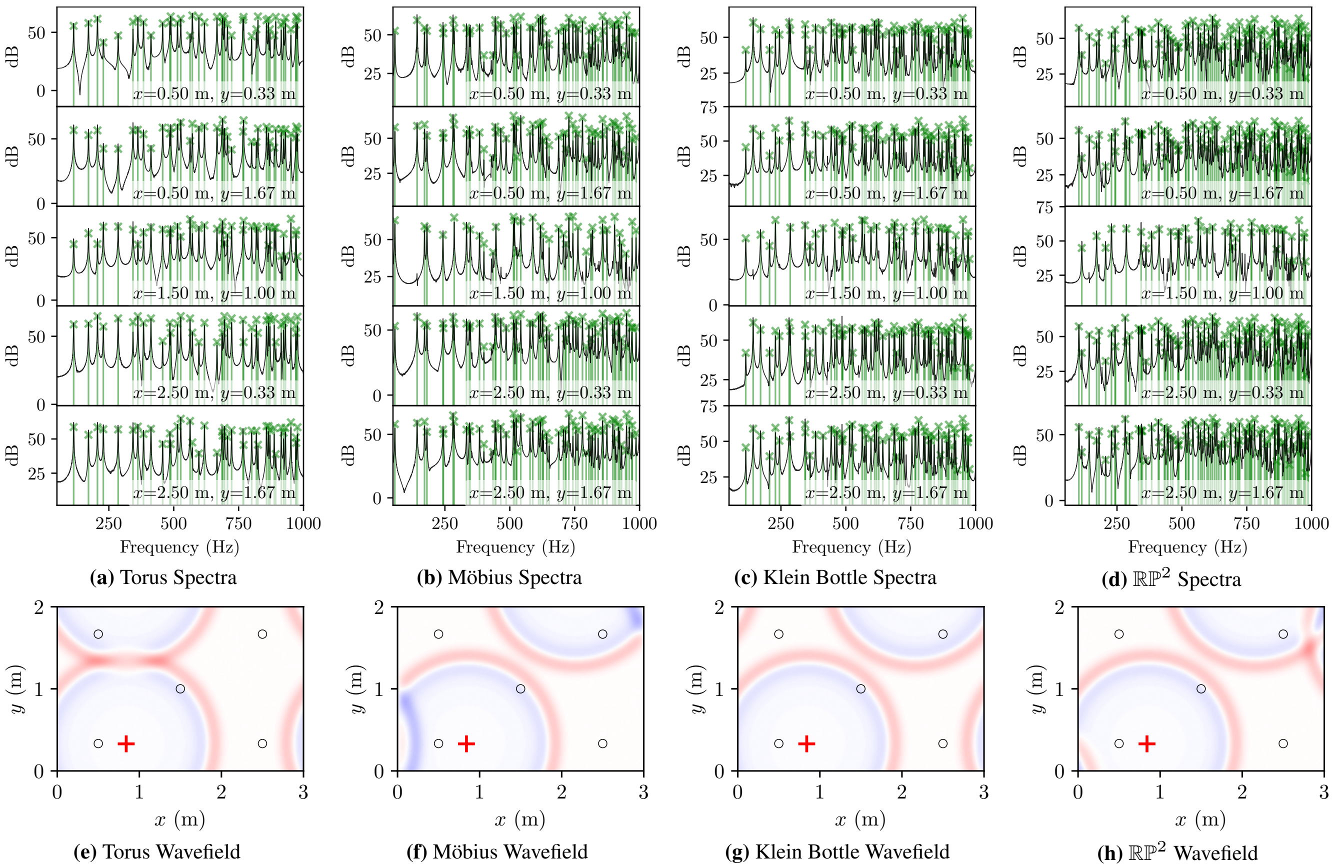

Figure 1: (a)-(d) Spectra of the modes for each manifold. Black solid lines indicate the spectrum of FDTD simulation up to 1 kHz. Green vertical lines indicate the theoretical mode frequencies f_{mn} and spatial mode amplitudes $\tilde{\phi}_{mn}$ with $L_x = 3.0$ m and $L_y = 2.0$ m, and the wave propagates in $c = 343$ m/s from a point source located at $x = 0.84$ m and $y = 0.33$ m to each receiver location indicated as legend in (a)-(d). (e)-(h) Simulated wavefields at a fixed time snapshot for each manifold, showing the spatial distribution of pressure corresponding to a superposition of modes excited by a point source shown as red plus + and received at the black circle ∘.

4. VERIFICATION BY FDTD SIMULATION

We verify the mode structures and eigenfrequencies derived in the previous section through numerical simulations. Specifically, we solve Equation (1) on the fundamental domain σ with the appropriate BCs corresponding to each manifold. The FDTD is computed on a uniform grid with spacing $h = 0.01$ m over the spatial domain $[0, L_x] \times [0, L_y]$. The scheme is written by $u_{ij}^{(n+1)} = 2u_{ij}^{(n)} - u_{ij}^{(n-1)} + (cT)^2 \Delta u_{ij}^{(n)}$ where the Laplacian is discretized by the standard five-point stencil

$$\Delta u_{ij} = \frac{u_{i+1,j} + u_{i-1,j} + u_{i,j+1} + u_{i,j-1} - 4u_{ij}}{h^2}, \tag{23}$$

where $cT = h/\sqrt{2}$, *i.e.*, the time step $T \approx 20.6\,\mu$s and a Nyquist frequency of $f_s/2 = 24.3$ kHz when $c = 343$ m/s. While the use of an explicit scheme in 2D FDTD can introduce some dispersion anisotropy, this is a well-known artifact, and validation is conducted within a range where it does not arise significantly. The initial condition is provided as a 2D Gaussian with zero velocity. The BCs are enforced using the ghost cells outside the domain before evaluating Equation (23) at the boundary points. The ghost cells are mirrored, with (or without) sign flips for the Dirichlet (or Neumann) cases. For the periodic BC, the ghost cells are rolled across the boundaries with (phase-conjugating) or without (torus) orientation flips as indicated by the colored arrows in Table 1.

Since the FDTD simulation is real-valued, the pressure field at a receiver effectively measures the real Green's function of the domain rather than a single eigenmode. The real Green's function at frequency f_{mn} is the sum of all eigenmode products over the degenerate subspace,

$$\tilde{\phi}_{mn}(\mathbf{r}_r, \mathbf{r}_s) = \left[\sum_k \big(\phi_k(\mathbf{r}_s) \cdot \phi_k(\mathbf{r}_r)\big)^2\right]^{\frac{1}{2}}, \tag{24}$$

where the summation runs over all eigenmodes k degenerate at frequency f_{mn}. A broadband Gaussian source at $\mathbf{r}_s$ excites each eigenmode with weight $\phi_k(\mathbf{r}_s)$, so the amplitude observed at $\mathbf{r}_r$ is proportional to this sum. One can verify that $\tilde{\phi}_{mn}$ depends on the relative displacement $\mathbf{r}_r - \mathbf{r}_s$ using the symmetry of the mode shapes and the addition theorems for the trigonometric functions.

Figure 1 (a–d) overlays the FDTD power spectrum with the analytic modal amplitudes in Equation (24) at five representative receiver positions. Peak frequencies of the FDTD spectrum agree with the analytic f_{mn} values to within the spectral resolution across all topologies, and the amplitude envelopes match within the 60 dB display range. Spectra for Dirichlet and Neumann rectangles are omitted for brevity.

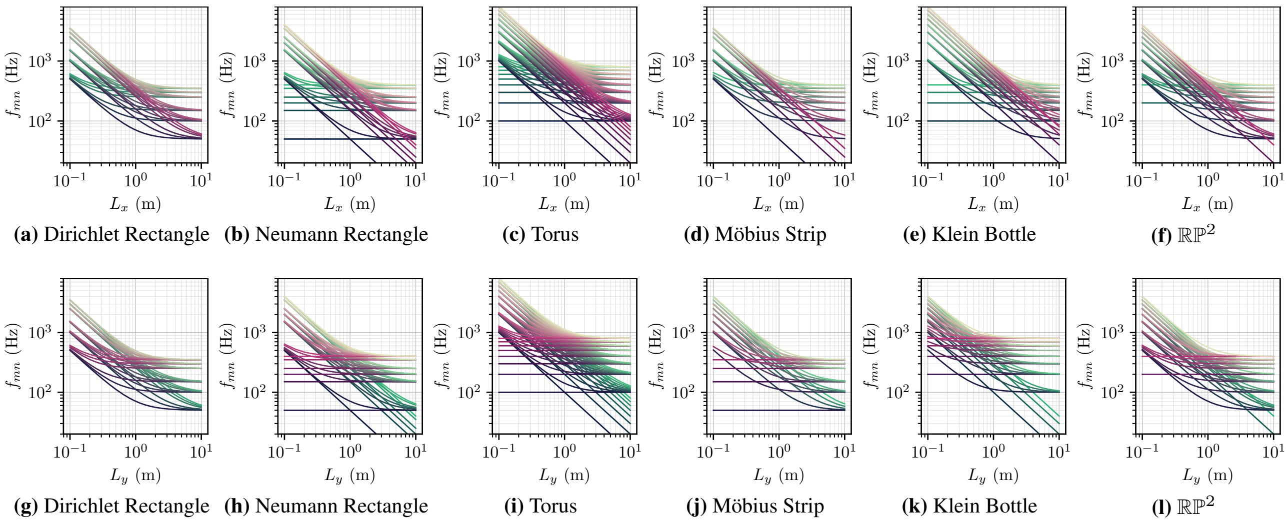

(a) Dirichlet Rectangle **(b)** Neumann Rectangle **(c)** Torus **(d)** Möbius Strip **(e)** Klein Bottle **(f)** $\mathbb{RP}^2$

(g) Dirichlet Rectangle **(h)** Neumann Rectangle **(i)** Torus **(j)** Möbius Strip **(k)** Klein Bottle **(l)** $\mathbb{RP}^2$

Figure 2: Mode frequencies as a function of L_x (top row) and L_y (bottom row) for each manifold. When varying L_x (or L_y) from 0.1 m to 10 m, L_y (or L_x) is fixed at 1.0 m. Each curve corresponds to a mode indexed by (m, n) for $m, n \leq 8$, with the color indicating each mode's index pair. Only f_{mn} with m, n where $\phi_{mn}(x, y) > 0$ are plotted, where $x = L_x/4$ and $y = 3L_y/4$. The speed of sound is chosen as $c = 100$ m/s for better visualization. Please refer to Figure 3 for identifying the mode index pairs corresponding to each color.

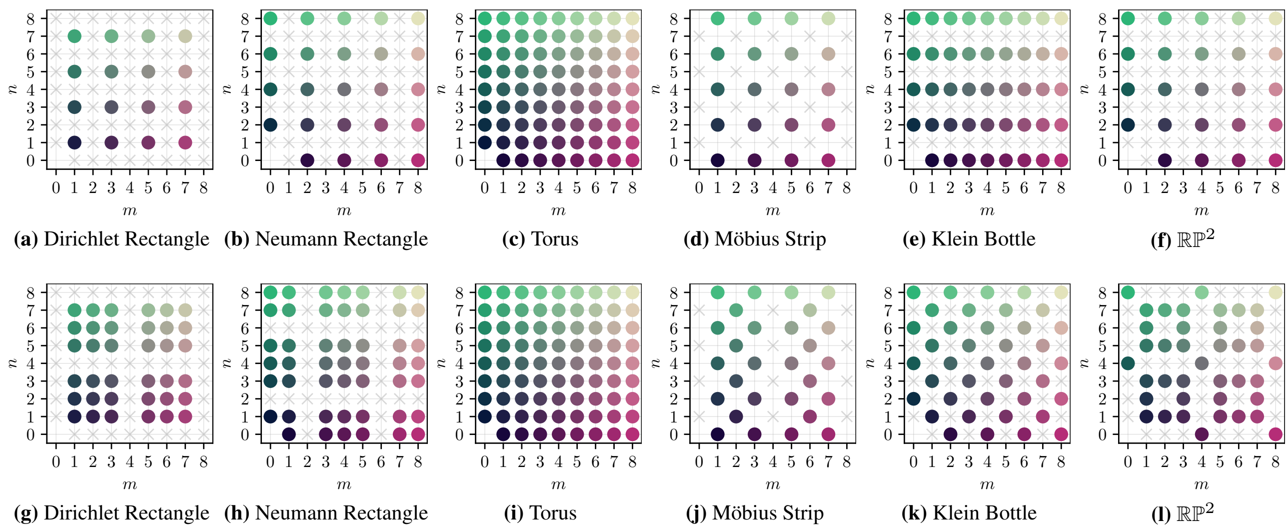

(a) Dirichlet Rectangle **(b)** Neumann Rectangle **(c)** Torus **(d)** Möbius Strip **(e)** Klein Bottle **(f)** $\mathbb{RP}^2$

(g) Dirichlet Rectangle **(h)** Neumann Rectangle **(i)** Torus **(j)** Möbius Strip **(k)** Klein Bottle **(l)** $\mathbb{RP}^2$

Figure 3: Valid combination of m and n for each manifold. Colored circles indicate the presence of a mode at the corresponding (m, n) index, while gray crosses indicate non-empty zero-magnitude indices, *i.e.*, (m, n) where $f_{mn} \geq 0$ but $\phi_{mn}(x, y) = 0$. (a)-(f) show the lattice of modes for $x = L_x/2$ and $y = L_y/2$. (g)-(l) show the lattice of modes for $x = L_x/4$ and $y = 3L_y/4$.

Table 2 quantifies the agreement between the analytic closed-form and FDTD modes (superscript cf and fd, resp.) by reporting the mean relative frequency error $\varepsilon_f = \frac{1}{M}\sum_{mn}|f^{\mathrm{cf}}_{mn} - f^{\mathrm{fd}}_{mn}|/f^{\mathrm{fd}}_{mn}$, and MAC $= \frac{1}{M}\sum_{mn}(\tilde{\phi}^{\mathrm{cf}}_{mn} \cdot \tilde{\phi}^{\mathrm{fd}}_{mn})^2/(\|\tilde{\phi}^{\mathrm{cf}}_{mn}\|^2\|\tilde{\phi}^{\mathrm{fd}}_{mn}\|^2)$, Modal Assurance Criterion, averaged for all M number of matched pairs (m, n). Numerical errors can arise from the finite approximations, and spectral leakage occurs contaminating the weak-amplitude peaks with the high noise floor of the sidelobes. To this end, a Hann window is applied at the cost of slightly widening the main-lobe width to 50 Hz. This is one of the primary causes of differences in MAC values between topologies. Yet, the mean relative frequency error is 0.02% for all cases, and the MAC values are close to 1.0.

Table 2: Modal validation for each boundary topology.

Topology	ε_f (%;↓)	MAC(↑)
Neumann	0.03	0.875
Dirichlet	0.03	0.944
Möbius strip	0.02	0.944
Torus	0.03	0.834
Klein's Bottle	0.02	0.932
Real Projective Plane	0.03	0.929

5. MODAL STRUCTURE OF THE BOUNDARIES

Figure 2 displays the mode frequencies as a function of the domain dimensions for each manifold, up to the 8th mode in each dimension. In each column, one dimension is held fixed while the other is varied; modes for which $\phi_{mn}(x_r, y_r) = 0$ at the receiver are excluded. Figure 3 provides a complementary plot for the lattice of allowed (m, n) pairs together with indicators of which modes vanish at the receiver, making explicit how the identification rules of each manifold constrain the admissible wavenumbers.

Modes invariant with respect to length. An obvious observation from Figure 2 is the presence of horizontal lines, *i.e.*, the modes whose frequency is independent of one dimension. These arise whenever $m = 0$ or $n = 0$ reduces the eigenfrequency formula to a single-axis expression. For the Dirichlet rectangle, $\sin(0)$ annihilates ϕ_{mn} when $m \cdot n = 0$, so no horizontal lines appear in either row. The same happens along the x axis of Möbius strip (see Figure 2 (d)). In all other geometries, neither zero-index is categorically forbidden. The presence of these length-invariant modes introduces aspect-ratio-dependent inharmonicity, *i.e.*, as L_x/L_y deviates from unity the invariant modes pull away from the rest of the spectrum, amplifying inharmonic beating. On the other hand, the Dirichlet rectangle converges to a perfectly harmonic spectrum at extreme aspect ratios, becoming close to a 1D string with integer harmonics.

Spectral density of the torus. Among all six geometries, the torus admits the densest set of modes. Its identification rules impose no parity constraint on either m or n, so every lattice point in $\mathbb{Z}^2$ is allowed (see Figure 3). As a result, Figure 2 shows the greatest number of distinct frequency curves for the torus. This density is further reflected in Figure 1: the torus spectrum displays the most uniformly populated set of peaks, with no systematic gaps, because no combination of indices is excluded and no receiver-position zero appears for generic listener locations.

Valid modes and asymmetry of non-orientable topology. As evident from Table 1, the f_{mn} of non-orientable manifolds are not very different from the orientable cases, but it is the identification rules *and* the mode shapes with $\phi_{mn} \neq 0$ (thus the set of allowed and non-zero-magnitude (m, n) combinations) that produce the most significant spectral differences. All modes with even $m + n$ are eliminated in $\mathcal{M}$, so every other diagonal of the frequency lattice is missing. Furthermore, the sine basis with m makes the modes at x vanish at every integer multiple of L_x/x (*e.g.*, $m = 0, 4, 8, \cdots$ for $x = L_x/4$), so the combination of non-zero modes becomes sparse and asymmetric across the two dimensions, producing a spectrum with fewer peaks and more inharmonic beating than the rectangle.

For $\mathcal{K}$, the cosine basis in x with a phase offset that depends on n produces a mode set that is distinct from all other cases, and the modes with $m = 0$ are uniform in x and therefore have double the energy of the other modes. Also, the x-spacing is halved relative to the rectangle, so the lowest x-only mode sits at $f = c/L_x$ instead of $c/(2L_x)$, pushing the x-modal ladder to higher frequencies and breaking the symmetry between the two spatial dimensions. This is evident from the f_{mn} formula of $\mathcal{K}$ with a factor of 4 on the m^2 term, which inherently introduces anisotropy in the spectrum. For $L_x \neq L_y$, this produces a frequency lattice with no rational substructure and the spectrum is inherently inharmonic regardless of dimension choice.

The $\mathbb{RP}^2$ spectrum is co-spectral with the Neumann rectangle, sharing the same frequency formula and full index set, but ϕ_{mn} are distinct due to the phase offsets in both directions, which couple m and n in a way that has no rectangle analogue. Similar to the Klein bottl, the phase offsets produce modes that are neither purely even nor purely odd, and the presence of both m and n in the phase offsets means that the parity of one index affects the mode shape in the other dimension, so the lattice of non-zero modes is not perfectly symmetric about the axes although the plot shown in Figure 3 only upto $m, n = 8$ does not make this asymmetry visually obvious. These features form a mode set that is distinct from all other cases despite identical frequencies, and $\mathbb{RP}^2$ can be audibly distinguished from a standard rectangle.

6. DISCUSSION AND FUTURE WORK

This study examines the acoustics of various 2D manifolds through a modal framework, and to ensure that these structures exhibit more natural reverberation when utilized as musical instruments, Rayleigh damping is applied while synthesizing the audio [1]. Thus, investigations on the geometries or damping ratios may be undertaken to extend the current sound synthesizer as a better musical instrument. One possible direction would be to generalize the currently surface-restricted formulation to cavity resonators of higher dimensions. For instance, in the case of a torus, it would be natural to consider its internal cavity in $\mathbb{R}^3$ filled with a medium such as air and analyze its resonance. However, for non-orientable manifolds, applying the same approach is not straightforward, as the non-orientability prevents a consistent definition of an interior and exterior. Consequently, a higher-dimensional framework may be required to model the acoustic characteristics that are analogous to the resonance of a cavity in 3D space. Also, extending the current analysis on 2D surfaces to a 3D non-orientable manifold, such as the real projective space $\mathbb{RP}^3$ or other 3-manifolds, would be a natural next step since the concept of the quotient space construction itself is not dimension-specific. Lastly, relaxing the assumption on the currently constant wave speed to a spatially varying $c(\mathbf{x})$ would model inhomogeneous media and, more subtly, could approximate the effect of intrinsic curvature of the manifold.

7. CONCLUSION

This paper presents an analysis of the acoustic modes for various boundary conditions by quotient space construction of the fundamental domain, and extends the analysis to the case of non-orientable 2D manifolds, including the Möbius strip, Klein bottle, and real projective plane. By deriving closed-form expressions for the eigenfrequencies and mode shapes, we have elucidated how the non-orientable topology imposes specific constraints on the allowed modes. The FDTD simulations on quotient spaces have verified these theoretical predictions, demonstrating spectral agreement between the simulated spectra and the analytic modal amplitudes across multiple receiver locations. Future work could extend this analysis to three-dimensional non-orientable manifolds, investigate the effects of inhomogeneous media and curvature, and explore the implications of these unique modal structures for musical acoustics applications. The authors hope that this work will inspire further exploration of the acoustic properties of non-orientable manifolds and their potential applications in sound synthesis and musical instrument design.

[1] Code and sound samples are available on https://kleinreverb.github.io/

8. REFERENCES

[1] J. O. Smith, *Physical Audio Signal Processing: For Virtual Musical Instruments and Audio Effects*, 2010 edition.

[2] V. Välimäki, J. Pakarinen, C. Erkut, and M. Karjalainen, "Discrete-time modelling of musical instruments," *Reports on Progress in Physics*, vol. 69, no. 1, pp. 1–78, 2006.

[3] L. E. Kinsler, A. R. Frey, A. B. Coppens, and J. V. Sanders, *Fundamentals of acoustics*. John Wiley & Sons, 2000.

[4] S. Bilbao, *Numerical Sound Synthesis: Finite Difference Schemes and Simulation in Musical Acoustics*. John Wiley & Sons, 2009.

[5] S. Bilbao, C. Desvages, M. Ducceschi, B. Hamilton, R. Harrison-Harsley, A. Torin, and C. Webb, "Physical modeling, algorithms, and sound synthesis: The ness project," *Computer Music Journal*, vol. 43, no. 2-3, pp. 15–30, 2019.

[6] M. Ducceschi, C. Touzé, S. Bilbao, and C. J. Webb, "Nonlinear dynamics of rectangular plates: investigation of modal interaction in free and forced vibrations," *Acta Mechanica*, vol. 225, no. 1, pp. 213–232, 2014.

[7] B. Bank and L. Sujbert, "Generation of longitudinal vibrations in piano strings: From physics to sound synthesis," *The Journal of the Acoustical Society of America*, vol. 117, no. 4, pp. 2268–2278, 2005.

[8] M. E. McIntyre, R. T. Schumacher, and J. Woodhouse, "On the oscillations of musical instruments," *The Journal of the Acoustical Society of America*, vol. 74, no. 5, 1983.

[9] M. Rau and J. Smith, "Measurement and modeling of a resonator guitar," in *Proceedings of the ISMA*, 2019.

[10] J. W. Lee, J. Park, M. J. Choi, and K. Lee, "Differentiable modal synthesis for physical modeling of planar string sound and motion simulation," *Advances in Neural Information Processing Systems*, vol. 37, pp. 1058–1081, 2024.

[11] G. P. Scavone, *An Acoustic Analysis of Single-reed Woodwind Instruments with an Emphasis on Design and Performance Issues and Digital Waveguide Modeling Techniques*. stanford university, 1997.

[12] L. Trautmann, S. Petrausch, and R. Rabenstein, "Physical modeling of drums by transfer function methods," in *2001 IEEE International Conference on Acoustics, Speech, and Signal Processing. Proceedings*, vol. 5. IEEE, 2001.

[13] J. Chowdhury, E. K. Canfield-Dafilou, and M. Rau, "Water bottle synthesis with modal signal processing," in *Int. Conf. Digital Audio Effects (DAFx)*, vol. 5, 2020.

[14] K. Xue, R. M. Aronson, J.-H. Wang, T. R. Langlois, and D. L. James, "Improved water sound synthesis using coupled bubbles," *ACM Transactions on Graphics (TOG)*, vol. 42, no. 4, 2023.

[15] J. W. Lee, G. S. An, J.-Y. Sun, and K. Lee, "Inverse nonlinearity compensation of dielectric elastomers for acoustic actuation," *IEEE Access*, vol. 12, pp. 164 792–164 802, 2024.

[16] C. Chafe, "Case studies of physical models in music composition," in *Proceedings of the 18th international congress on acoustics*, 2004, pp. 2505–2508.

[17] J. Bělín, T. Tyc, and S. Horsley, "Optical simulation of quantum mechanics on the möbius strip, klein's bottle and other manifolds, and talbot effect," *New Journal of Physics*, vol. 23, no. 3, p. 033003, 2021.

[18] D. Bartolo and D. Carpentier, "Topological elasticity of nonorientable ribbons," *Physical Review X*, vol. 9, no. 4, p. 041058, 2019.

[19] A. Thonikkadavan, M. d'Aquino, and R. Hertel, "Rotating spin wave modes in nanoscale möbius strips," *npj Spintronics*, vol. 4, no. 1, p. 4, 2026.

[20] J. K. Hamilton, I. R. Hooper, and C. R. Lawrence, "Absorption modes of möbius strip resonators," *Scientific Reports*, vol. 11, no. 1, p. 9045, 2021.

[21] A. Dodik, I. Yu, K. Chandra, J. Ragan-Kelley, J. Tenenbaum, V. Sitzmann, and J. Solomon, "Meschers: Geometry processing of impossible objects," *ACM Transactions on Graphics (TOG)*, vol. 44, no. 4, pp. 1–10, 2025.

9. APPENDIX: EQUIVARIANCE CONDITIONS

Möbius Strip. Using $\sin(k_x x + m\pi) = (-1)^m \sin(k_x x)$ and $e^{in\pi} = (-1)^n$, Equation (12) is verified by expanding the two arguments separately:

$$\begin{aligned}
&\phi_{mn}(x+L_x, y+L_y) \\
&\quad= \sqrt{\frac{2}{L_x L_y}} \sin\left(\frac{m\pi x}{L_x} + m\pi\right) \exp\left(\frac{i\pi n y}{L_y} + in\pi\right) \\
&\quad= (-1)^m \sqrt{\frac{2}{L_x L_y}} \sin\left(\frac{m\pi x}{L_x}\right) \cdot (-1)^n \exp\left(\frac{i\pi n y}{L_y}\right) \\
&\quad= (-1)^{m+n}\, \phi_{mn}(x, y). \qquad (25)
\end{aligned}$$

Comparing Equation (25) with Equation (12) gives the constraint $(-1)^{m+n} = -1$, which holds if and only if $m + n$ is odd.
Klein Bottle. Using $\cos(\theta + n\pi/2) = (-1)^n \cos(\theta - n\pi/2)$, Equation (15) is verified as

$$\begin{aligned}
\phi_{mn}(-x,\, y+L_y) &= A_{\mathcal{K}} \cos\left[\frac{-2m\pi x}{L_x} - \frac{n\pi}{2}\right] e^{i\pi n y/L_y} e^{in\pi} \\
&= (-1)^n A_{\mathcal{K}} \cos\left[\frac{2m\pi x}{L_x} - \frac{n\pi}{2}\right] e^{i\pi n y/L_y} \\
&= (-1)^n \phi_{mn}(x, y).
\end{aligned}$$

$A_{\mathcal{K}}$ denotes the normalization factor $\sqrt{2/(L_x L_y^{(1)})}$.
Real Projective Plane. Using $\cos(\theta + n\pi/2) = (-1)^n \cos(\theta - n\pi/2)$, Equation (19) is verified as

$$\begin{aligned}
\phi_{mn}(x+L_x, -y) &= A_{\mathbb{RP}^2} \cos\left[\tfrac{m\pi x}{L_x} + m\pi - \tfrac{(m+n)\pi}{2}\right] \\
&\qquad \cos\left[-\tfrac{n\pi y}{L_y} + \tfrac{(m+n)\pi}{2}\right] \\
&= (-1)^m A_{\mathbb{RP}^2} \cos\left[\tfrac{m\pi x}{L_x} - \tfrac{(m+n)\pi}{2}\right] \\
&\qquad (-1)^{m+n} \cos\left[\tfrac{n\pi y}{L_y} + \tfrac{(m+n)\pi}{2}\right] \\
&= (-1)^n \phi_{mn}.
\end{aligned}$$

$A_{\mathbb{RP}^2}$ denotes the normalization factor $\sqrt{2/(L_x^{(1)} L_y^{(1)})}$. Equation (20) follows symmetrically, giving $(-1)^m \phi_{mn}$.